# Developing mixed convection flow in a horizontal tube under circumferentially non-uniform heating

D. K. CHOI and D. H. CHOI

Korea Advanced Institute of Science and Technology, 373-1 Kusong-dong, Yusung-gu,
Taejon 305-701, Korea

**Abstract**—The developing process of the mixed convection flow in a circular tube, the lower half of which is maintained at the constant heat-flux condition, is examined. Using a fully elliptic Navier–Stokes procedure, which is made to satisfy global mass continuity at each interior section, calculations have been performed for $Pr = 0.7$ and 5 at $Re = 250$. For $Gr$ between $10^6$ and $10^7$, the vortical secondary flow develops almost immediately and increases the heat transfer considerably. The active crossflow motion can cause the flow in the upper region to reverse early in the developing region. The natural developed flow is of two-vortex type. However, as the temperature gradient builds up near the bottom surface, a new pair of vortices could be developed. The flow, in the present parameter range, is shown to develop either type of solution. The four-vortex solution is more likely to occur as $Pr$ and/or $Gr$ increase(s). The details of the developing process are presented.

## INTRODUCTION

IT IS well known that gravity plays an important role in characterizing mixed convection duct flows. If the orientation of the duct is not vertical, the buoyancy force induces the secondary flow, which enhances heat transfer between the wall and the fluid. Such effects are most pronounced in horizontal flows and there have been numerous studies for various enclosure shapes and thermal boundary conditions.

Most of the studies in the literature on laminar mixed convection in a horizontal duct have been concerned with the developed conditions [1–4]. Nandakumar *et al.* [4] examined the flows in circular and square ducts for axially uniform heat-flux and circumferentially isothermal boundary conditions. A dual solution exists for a certain range of Grashof number (*Gr*) as the Dean problem [5, 6] in the isothermal curved tubes, i.e. both two- and four-vortex crossflow patterns are possible. There have also been studies for non-uniform circumferential boundary conditions. Patankar *et al.* [7] treated the mixed convection flow in a circular tube with the top half insulated while the bottom half was heated at a specified rate. They observed a change in the flow pattern from a two-vortex type to a four-vortex one as *Gr* increases. However, they did not report dual solutions. Law *et al.* [8] reexamined the problem in a search for the multiple solution. Among the three geometric shapes they studied, i.e. square, circular and semicircular ducts, with the thermal boundary conditions similar to those in Patankar *et al.*, dual solutions were obtained in square and semicircular ducts. For the circular duct, however, only the two-vortex solution could be found for the

entire Grashof number range of their study ($2/\pi$ $Gr < 10^5$–$10^6$). This finding is in contradiction to that of Patankar *et al.*, whose solution exhibits a four-vortex pattern above a certain critical Grashof number. On the other hand, the recent study by the present authors [9] for the circular duct with the same boundary conditions revealed that the dual solution does exist for the wide range of Prandtl number ($0.2 \leqslant Pr \leqslant 10$); it also identified the lower end of the dual solution region $Gr_{crit}$ for the given Prandtl number.

However, it was still unclear how the flow develops eventually to these two different final states. This developing process would not only provide some insights into the complicated physics involved, but legitimize the fully developed solution, i.e. the solution is not fictitious but physically obtainable. The subject of developing 3-D flow has been relatively unexplored [10–16]. Moreover, among the handful that have been reported, many adopted some sort of simplification to alleviate computational efforts: either invoking the large Prandtl number approximation to eliminate non-linear inertia terms in the momentum equations [10] or parabolizing the equations in the streamwise direction [11–14]. Obviously these approximations cannot be applied to a broad class of flow: the parabolic assumption is valid only for relatively small Grashof number flows since a strong buoyancy force may cause the flow to reverse [16]. The works of Hishida *et al.* [15] and Yam and Dwyer [16] did not use either of the above assumptions. However, the isothermal wall condition in their study reduces the buoyancy force with increasing axial position and made the

## NOMENCLATURE

| | | | | |
|---|---|---|---|---|
| $C_f$ | local friction factor, equation (28) | | $Z^*$ | inverse Graetz number $(= z/D\,Re\,Pr)$ |
| $D$ | tube diameter | | $z$ | axial coordinate. |
| $f$ | Fanning friction factor, equation (26) | | | |
| $Gr$ | Grashof number, equation (23) | | **Greek symbols** | |
| $g$ | gravity | | $\alpha$ | thermal diffusivity |
| $k$ | thermal conductivity | | $\beta$ | thermal expansion coefficient |
| $Nu$ | local Nusselt number, equation (28) | | $\eta$ | dimensionless radial coordinate |
| $P$ | dimensionless pressure, equation (23) | | $\theta$ | azimuthal coordinate |
| $p$ | pressure | | $v$ | kinematic viscosity |
| $Pr$ | Prandtl number, equation (23) | | $\rho$ | density |
| $Q'$ | rate of heat transfer per unit length | | $\Phi$ | dimensionless temperature, equation (23) |
| $q$ | rate of heat transfer per unit area | | $\tau_w$ | wall shear stress in the $z$-direction. |
| $R$ | tube radius | | | |
| $Re$ | Reynolds number | | **Subscripts** | |
| $r$ | radial coordinate | | 0 | forced convection value |
| $T$ | temperature | | b | bulk property |
| $U, V, W$ | dimensionless velocities, equation (23) | | in | inlet value |
| | | | w | wall value. |
| $u, v, w$ | velocity components in $r, \theta, z$ directions | | **Others** | |
| $Z$ | dimensionless axial coordinate | | $^-$ | section average. |

analysis fairly simple; the secondary motion vanishes as the flow becomes fully developed. Hishida *et al.* [17] later examined the flow development in a horizontal tube with the uniform heat flux condition for moderate Grashof numbers; no multiplicity of the solution was observed.

The purpose of this study is to investigate the development of the primary/secondary flow, their effects on heat transfer, and bifurcation to those two different final states in a circular tube, which is insulated on the top half and heated on the bottom half. A clear picture of this developing process will also validate the fully developed solutions obtained earlier [9]. To accomplish this, we simulate the flow by the 3-D fully elliptic Navier–Stokes and energy equations: the SIMPLER algorithm of Patankar [18] is modified to have the velocity and pressure fields satisfy the global continuity at every streamwise location. The scheme is found to be efficient and robust even when a large region of reversed flow is present.

## SOLUTION PROCEDURE

### Modified SIMPLER

During the iteration cycle of SIMPLER, the continuity generally is not satisfied and the overall mass conservation can be achieved only after the solution is completely converged. In other words, the outlet mass flux may not be in balance with the inlet mass flux at a given iteration. This is physically incorrect

and degrades the efficiency of the algorithm. To get around this difficulty, one could either add (subtract) a fixed amount of velocity at the exit or make the exit velocity proportionally larger (smaller) to match the mass flux at both ends [19, 20]. Even with this correction, the global continuity at interior sections is still lacking. The correction of pressure which depends on the velocity cannot therefore be very efficient. Here, we will present a fully elliptic method, which is based on the 3-D parabolic algorithm of Raithby and Schneider [21], that satisfies continuity in average sense at every station.

The dimensionless equations of continuity and momentum for incompressible 3-D flows in Cartesian coordinates are written as follows:

$$\frac{\partial u}{\partial x} + \frac{\partial v}{\partial y} + \frac{\partial w}{\partial z} = 0, \tag{1}$$

$$\frac{\partial}{\partial x}(uu) + \frac{\partial}{\partial y}(vu) + \frac{\partial}{\partial z}(wu) = -\frac{\partial p}{\partial x} + \frac{1}{Re}\nabla^2 u, \tag{2}$$

$$\frac{\partial}{\partial x}(uv) + \frac{\partial}{\partial y}(vv) + \frac{\partial}{\partial z}(wv) = -\frac{\partial p}{\partial y} + \frac{1}{Re}\nabla^2 v, \tag{3}$$

$$\frac{\partial}{\partial x}(uw) + \frac{\partial}{\partial y}(vw) + \frac{\partial}{\partial z}(ww) = -\frac{\partial p}{\partial z} + \frac{1}{Re}\nabla^2 w, \tag{4}$$

where $u, v, w$ are velocity components in $x$-, $y$- and $z$-directions, respectively, $p$ the pressure and $Re$ the Reynolds number. The $z$-coordinate corresponds to the streamwise direction.
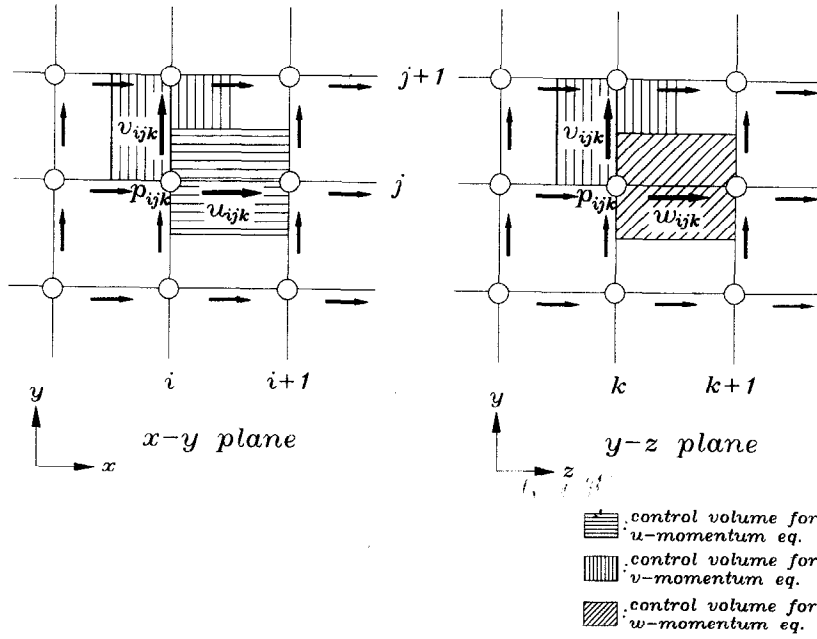
FIG. 1. Staggered grid.

Integration of these equations over the appropriate control volume for node $i, j, k$ in a staggered grid system (see Fig. 1) gives the following discretized equations:

$$A_p^u u_{ijk}^* = \sum A_{nb}^u u_{nb}^* + (p_{ijk}^* - p_{i+1jk}^*)\Delta y \Delta z + S^u, \quad (5)$$

$$A_p^v v_{ijk}^* = \sum A_{nb}^v v_{nb}^* + (p_{ijk}^* - p_{ij+1k}^*)\Delta z \Delta x + S^v, \quad (6)$$

$$A_p^w w_{ijk}^* = \sum A_{nb}^w w_{nb}^* + (p_{ijk}^* - p_{ijk+1}^*)\Delta x \Delta y + S^w, \quad (7)$$

where:

$$\sum A_{nb}^\phi \phi_{nb} = A_e^\phi \phi_{i+1jk} + A_w^\phi \phi_{i-1jk} + A_n^\phi \phi_{ij+1k}$$

$$+ A_s^\phi \phi_{ij-1k} + A_d^\phi \phi_{ijk+1} + A_u^\phi \phi_{ijk-1}. \quad (8)$$

Following SIMPLER, the pressure $p^*$ is computed from the Poisson-like pressure equation, which is obtained by coupling the momentum and continuity equations. For the velocity and pressure fields to satisfy the global continuity, the following corrections are made at each cross-section:

$$p_{ijk+1} = p_{ijk+1}^* + \delta p_{k+1}, \quad (9)$$

$$w_{ijk} = w_{ijk}^* + \delta w_{ijk}. \quad (10)$$

It should be noted that the correction for the velocity varies over the cross-section while that for the pressure is constant in the plane. The rationale for doing so is that, since $p^*$ is obtained from the elliptic equation, its gradient in the cross-section is considered accurate. Only the axial pressure gradient which governs mass flux through the plane needs to be corrected. In terms of these new velocity and pressure, the streamwise momentum equation may also be written as

$$A_p^w w_{ijk} = A_e^w w_{i+1jk} + A_w^w w_{i-1jk} + A_n^w w_{ij+1k} + A_s^w w_{ij-1k}$$

$$+ A_u^w w_{ijk-1} + A_d^w w_{ijk+1}^* + (p_{ijk} - p_{ijk+1})\Delta x \Delta y + S^w. \quad (11)$$

The velocity at $k+1$ is still unknown and, hence, $w^*$ is used in place of $w$. Subtracting equation (7) from (11) and noting that $\delta w_{k-1} = \delta p_k = 0$ since $w_{k-1}$ and $p_k$ have already been corrected at station $k$, we obtain:

$$A_p^w \delta w_{ijk} = A_e^w \delta w_{i+1jk} + A_w^w \delta w_{i-1jk} + A_n^w \delta w_{ij+1k}$$

$$+ A_s^w \delta w_{ij-1k} - \delta p_{k+1} \Delta x \Delta y, \quad (12)$$

or

$$A_p^w f_{ij} = A_e^w f_{i+1j} + A_w^w f_{i-1j} + A_n^w f_{ij+1}$$

$$+ A_s^w f_{ij-1} - \Delta x \Delta y, \quad (13)$$

where

$$f_{ij} = \frac{\partial w_{ijk}}{\partial p_{k+1}}. \quad (14)$$

This equation is similar to that of Pratap's [22] except the first four terms in the right-hand side which are not accounted for in his method. These terms represent the ellipticity of the velocity correction in the plane; these are crucial in making the present procedure more efficient and robust as is the difference of SIMPLER from SIMPLE (in SIMPLE, the pressure field is obtained from the pressure correction equation rather than solving the pressure equation directly) [18]. The boundary condition for equation (13) is either $f = 0$ or $\partial f / \partial n = 0$ depending on whether the velocity or
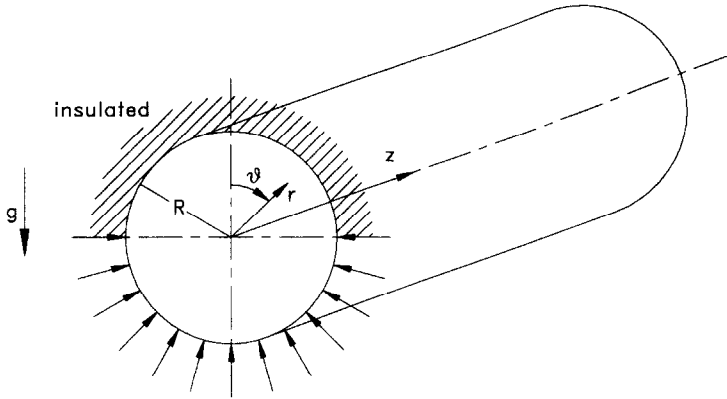
FIG. 2. Coordinate system.

the velocity gradient is specified along the boundary. Equations (10) and (14) then give:

$$w_{ijk} - w_{ijk}^* = f_{ij}\delta p_{k+1}. \tag{15}$$

The bulk pressure correction is obtained to satisfy global continuity as:

$$\delta p_{k+1} = \frac{Q - Q^*}{\sum_i \sum_j f_{ij}\Delta x\,\Delta y}, \tag{16}$$

where $Q$ is the correct volume flux through the cross-section $k$ and $Q^*$ the volume flux corresponding to $w^*$.

This procedure gives the mass flux through section $k$ which is equal to that through the inlet plane; it is summarized below.

(1) Solve the pressure equation over the entire domain to get $p^*$.
(2) Using $p^*$, $u^*$ and $v^*$ are obtained from equations (5) and (6).
(3) $w^*$ is calculated by equation (7).
(4) $w$ and $p$ are corrected to satisfy the global continuity.
(5) Steps (3) and (4) are repeated until the axial momentum and global continuity equations at $k$ are satisfied (two–three iterations appear to be sufficient for the flows tested).
(6) Repeat steps (3)–(5) until the exit plane is reached.
(7) Solve the pressure correction equation; the velocity components $u$, $v$ and $w$ are corrected over the whole domain (the pressure is not updated in this step).
(8) Return to step (1) unless the desired convergence criteria are met.

*Mixed convection in the entrance region of a horizontal duct*

For a developing mixed convection flow in a heated horizontal circular tube, invoking the Boussinesq approximation, the dimensionless governing equations of continuity, momentum and energy are written in the cylindrical coordinate system $(r, \theta, z)$ shown in Fig. 2:

$$\frac{1}{\eta}\frac{\partial}{\partial \eta}(\eta U) + \frac{1}{\eta}\frac{\partial V}{\partial \theta} + \frac{\partial W}{\partial Z} = 0, \tag{17}$$

$$U\frac{\partial U}{\partial \eta} + \frac{V}{\eta}\frac{\partial U}{\partial \theta} + W\frac{\partial U}{\partial Z} - \frac{V^2}{\eta} = -\frac{\partial P}{\partial \eta}$$
$$+ \frac{1}{Re}\left(\nabla^2 U - \frac{2}{\eta^2}\frac{\partial V}{\partial \theta} - \frac{U}{\eta^2}\right) + \frac{8Gr}{Re^2}\Phi\cos\theta, \tag{18}$$

$$U\frac{\partial V}{\partial \eta} + \frac{V}{\eta}\frac{\partial V}{\partial \theta} + W\frac{\partial V}{\partial Z} + \frac{UV}{\eta} = -\frac{1}{\eta}\frac{\partial P}{\partial \theta}$$
$$+ \frac{1}{Re}\left(\nabla^2 V + \frac{2}{\eta^2}\frac{\partial U}{\partial \theta} - \frac{V}{\eta^2}\right) - \frac{8Gr}{Re^2}\Phi\sin\theta, \tag{19}$$

$$U\frac{\partial W}{\partial \eta} + \frac{V}{\eta}\frac{\partial W}{\partial \theta} + W\frac{\partial W}{\partial Z} = -\frac{\partial P}{\partial Z} + \frac{1}{Re}\nabla^2 W, \tag{20}$$

$$U\frac{\partial \Phi}{\partial \eta} + \frac{V}{\eta}\frac{\partial \Phi}{\partial \theta} + W\frac{\partial \Phi}{\partial Z} + 4W/(\pi Re Pr) = \frac{1}{Re Pr}\nabla^2 \Phi, \tag{21}$$

where

$$\nabla^2 = \frac{1}{\eta}\frac{\partial}{\partial \eta}\left(\eta\frac{\partial}{\partial \eta}\right) + \frac{1}{\eta^2}\frac{\partial^2}{\partial \theta^2} + \frac{\partial^2}{\partial Z^2}, \tag{22}$$

and the dimensionless variables are defined as:

$$\eta = r/D \quad Z = z/D \quad Re = w_{in}D/v \quad Pr = v/\alpha$$
$$U = u/w_{in} \quad V = v/w_{in} \quad W = w/w_{in}$$
$$P = p/\rho w_{in}^2 \quad \Phi = \frac{T - T_b}{Q'/k} \quad Gr = g\beta Q' R^3/kv^2. \tag{23}$$

Since the flow is symmetric, it suffices to consider only half the tube cross-section $(0 \leqslant \theta \leqslant \pi)$. The boundary conditions may then be expressed as:

inlet:
$$U = V = \Phi = 0 \quad W = 1$$

outlet:

$$\frac{\partial^2 U}{\partial Z^2} = \frac{\partial^2 V}{\partial Z^2} = \frac{\partial^2 W}{\partial Z^2} = \frac{\partial^2 \Phi}{\partial Z^2} = 0$$

$\eta = 0.5$:

$$U = V = W = 0 \quad \text{(no-slip)}$$

$\eta = 0.5, \quad 0 \leqslant \theta \leqslant \frac{\pi}{2}$:

$$\frac{\partial \Phi}{\partial \eta} = 0 \quad \text{(adiabatic)}$$

$\eta = 0.5, \quad \frac{\pi}{2} \leqslant \theta \leqslant \pi$:

$$\frac{\partial \Phi}{\partial \eta} = \frac{2}{\pi} \quad \text{(uniform heat flux)}$$

$\theta = 0, \theta = \pi$:

$$V = 0 \quad \frac{\partial U}{\partial \theta} = \frac{\partial W}{\partial \theta} = \frac{\partial \Phi}{\partial \theta} = 0. \quad \text{(symmetry)} \quad (24)$$

These equations are discretized on a staggered grid by integrating the governing equations over control volumes. The QUICK scheme of Leonard [23] is adopted for the convective terms to reduce the error due to numerical diffusion whereas the central differencing is used for other derivatives. The equations are solved iteratively by using the modified SIMPLER algorithm described above and the solution is considered converged when the following criteria are met:

$$\text{Max}\,(|Res_Q|) < 10^{-4}$$

$$(Q : \text{continuity}, U, V, W, \Phi \text{ equations})$$

$$|Q^{n+1} - Q^n|/|Q^n| < 5 \times 10^{-5} \quad (Q : fRe \text{ and } \overline{Nu}).$$

$$(25)$$

## RESULTS AND DISCUSSION

Before proceeding further with the present procedure, modified SIMPLER, two sets of calculation have been performed to verify its efficiency: a channel entrance region and a backward facing step of 2 to 1 expansion. The convergence behavior for various Reynolds numbers is compared with that of the standard SIMPLER algorithm in Fig. 3. Here, we confine ourselves to 2-D flows to save computational effort. The 3-D flow with a large region of reversed flow can also be treated efficiently as shall be seen later in this section.

For comparison, the initial and boundary conditions are kept the same for both algorithms. The hybrid scheme in Patankar [18] is used for convective and diffusive derivatives and the relaxation factor is fixed at 0.8 for the momentum equations. Two solutions are identical when converged as the same differencing scheme has been adopted; the accuracy of the method was verified, although the comparison is not shown here, against the parabolic solution for the developing flow in a tube reported earlier [14]. The convergence history of the channel flow is shown in Fig. 3a. Here, $Res_c$ denotes the sum of the absolute errors in the continuity equation over the whole domain. As seen in the figure, the present algorithm is superior to SIMPLER for all Reynolds numbers tested. The number of iteration required seems nearly independent of the Reynolds number for the present algorithm while that of the existing algorithm is adversely affected by the increasing Reynolds number. It should be noted that the run time per iteration is almost the same for both methods. A similar trend is observed in Fig. 3b for the backward facing step flow despite the large recirculating region. The degree of improvement, however, is relatively small. Nevertheless the modification is still quite satisfactory as the iteration number is reduced by the factor of 1.5–2.7 for the range of Reynolds number tested.

The calculations for the entrance region of a horizontal tube have been performed for two Prandtl numbers, 0.7 and 5, at a fixed Reynolds number of 250. The Grashof number is chosen to vary up to $10^7$ as the fully developed flow has dual solutions at these Grashof numbers [9]. A few different computational grids were tested for $Pr = 0.7$ and $Gr = 10^7$ to confirm that the solution is grid independent. A $30 \times 30 \times 60$ grid which is uniform in the circumferential direction and densely distributed near the wall and the inlet was found adequate and has been used throughout in the present study.

To gain insight of the global picture of the flow, the Fanning friction factor and the average Nusselt number distribution along the tube are presented in Fig. 4. The friction factor $f$ is deduced from the force balance and is given by:

$$f = \frac{(-d\bar{p}/dz)D}{\frac{1}{2}\rho\bar{w}^2}, \quad (26)$$

where $\bar{p}$ is the mean pressure in the section and the average Nusselt number at the section is defined as:

$$\overline{Nu} = \frac{qD}{k(\bar{T}_w - T_b)} \quad \bar{T}_w = \frac{1}{\pi}\int_{\pi/2}^{3\pi/2} T_w \, d\theta. \quad (27)$$

These two quantities are normalized by the values of the fully developed forced convection flow and shown in the figure.

Near the inlet, the buoyancy force is yet to be developed and all the curves follow that of the forced convection flow. As $Z$ increases, however, the buoyancy effects become noticeable and each curve starts to deviate from the limiting curve. The buoyancy force induces secondary flow and the resulting mixing increases the flow resistance and heat transfer between the wall and the fluid. The buoyancy effects become larger as $Gr$ increases: the deviation from the forced convection value grows and the point where it starts moves upstream. The developing process is quite complex as the primary and the secondary flows are fully coupled: $fRe$ and $Nu$ oscillate until the flow gets fully developed and this will be brought up again later in the discussion.
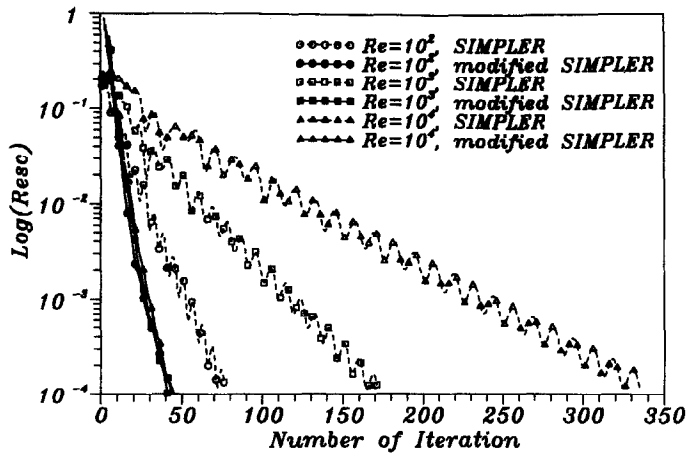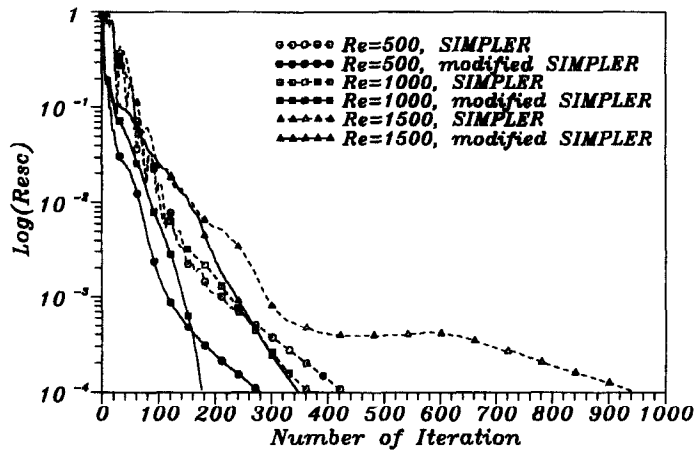
FIG. 3. Convergence history: (a) channel flow; and (b) step flow.

Bifurcation to four-vortex solution occurs when the flow is near fully developed and is less dependent on $Gr$ for $Pr = 0.7$ whereas, for $Pr = 5$, it occurs earlier in the developing stage and the point of its occurrence moves upstream as $Gr$ increases. This is, as we shall see later, due to the steeper unstable temperature gradient in the bottom region for $Pr = 5$ caused by a thinner thermal boundary layer.

The developing process can be better illustrated from the crossflow patterns: isotherms, crossflow velocity vectors, isovels of the axial flow, and isobars at various sections are presented in the next few figures. Here, unless noted otherwise, the contours are drawn at equal increment and the reference values are given in the final cross-section. Figure 5 shows the two-vortex solution of $Pr = 0.7$ at $Gr = 10^6$. At $Z^* = 2 \times 10^{-3}$, which is approximately only one-half the diameter of the tube, the buoyancy driven secondary flow has already been visibly developed especially near the heated surface. The phenomenon

is still local in nature and the small inward motion in the upper half of the tube is due primarily to the growth of the boundary layer. The temperature distribution suggests that the heat transfer is mostly conductive; the axial velocity exhibits predominantly forced-convection-flow behavior. This is the point where the friction factor and the Nusselt number start to deviate from the forced convection values seen in Fig. 4. As $Z$ increases the secondary motion becomes stronger: the colder fluid in the core region moves downward to fill the void and a clear vortical flow pattern emerges. The downward movement of the high momentum fluid in the core region makes the maximum axial velocity occur somewhat below the center: the flow in the lower part accelerates slightly while that in the upper half decelerates. As the trend continues, a small region of axial flow reversal appears near the symmetry plane along the top surface ($Z^* = 6.5 \times 10^{-3}$) and we will get back to this point later.
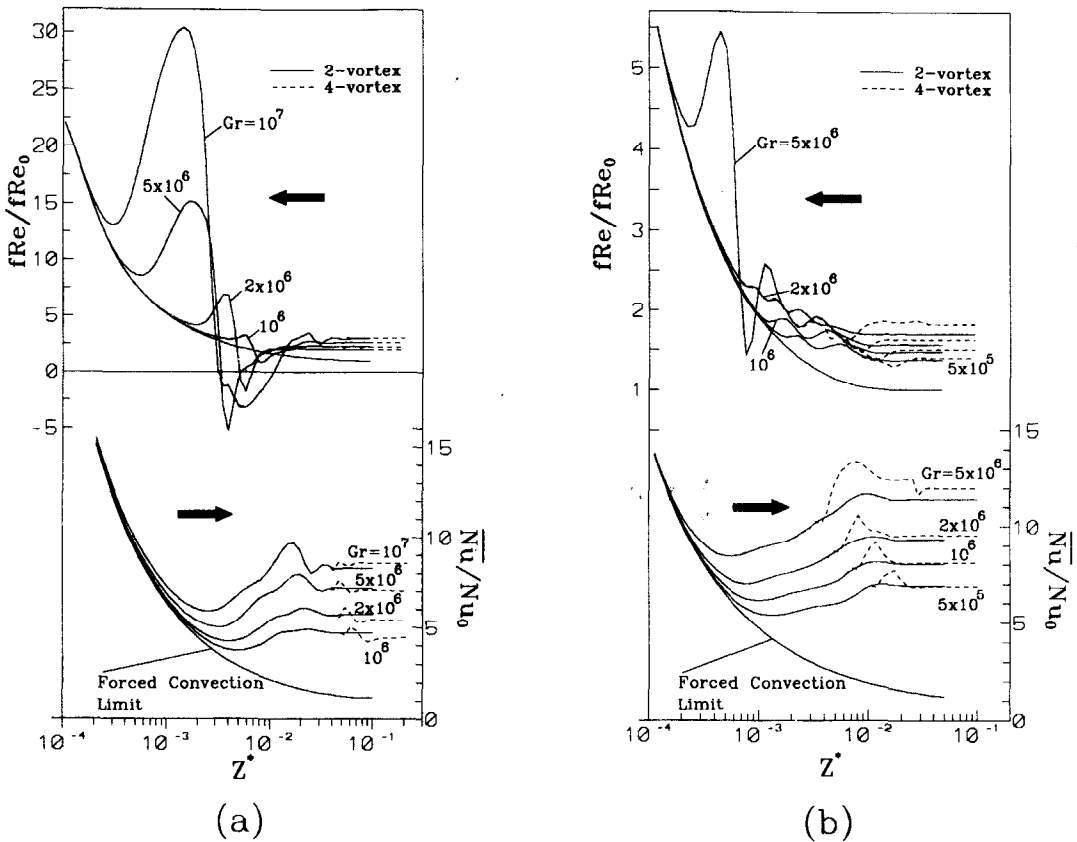
FIG. 4. Axial variation of Fanning friction factor and average Nusselt number: (a) $Pr = 0.7$; and (b) $Pr = 5$.

The heat transfer in the cross-section is handsomely enhanced by this mixing action. The average Nusselt number does not rise immediately, however, because the growing thermal boundary layer hinders the heat transfer. The balance between these two effects is reached at $Z^* \approx 5 \times 10^{-3}$ and hence occurs the minimum of $\overline{Nu}$ (Fig. 4). The mixing, on the other hand, makes the temperature more uniform and thus dampens the secondary motion. The oscillatory behavior of $f$ and $Nu$ in Fig. 4 is an evidence of this process. A similar phenomenon was also observed and discussed in Mahaney *et al.* [13] for a rectangular duct flow.

The developing process of a higher $Gr$ ( $= 10^7$) is shown next in Fig. 6. The secondary motion in this case is much stronger, which is expected, and also the flow exhibits very different initial behavior: the pressure variation in the cross-section is much larger and the longitudinal boundary-layer growth is more uneven. The boundary layer thickens rapidly along the region near $\theta = 0$, which can be seen from axial velocity distribution; the secondary flow appears to be initiated by this growing boundary layer and the considerable pressure difference between the upper and lower regions. This is apparent at $Z^* = 10^{-3}$ where the main direction of flow is downward. This

crossflow motion accelerates the axial flow in the lower half and retards it in the upper region. A region of reversed flow soon appears along the top surface ($Z^* = 10^{-3}$), which, although not as large, was also spotted in the earlier case. This may be attributed to the adverse pressure gradient shown in Fig. 7: the pressure gradient along $\theta = 0$ is, in general, less favorable than elsewhere at the outset and eventually becomes adverse before it assumes the fully developed value. The flow reversal makes the fluid in the upper region hotter than that below, especially in the first few cross-sections, because of the convective heat transfer from the downstream fluid.

Farther downstream, the buoyancy driven secondary flow penetrates to the upper region along the tube surface and the region of reversed flow diminishes gradually. This brings the vortical motion upward and the strong upward flow forms a new vortex in the upper region. The original vortex, although weakened, remains at its original position and these two corotating vortices, which are connected through a saddle point, coexist briefly before the upper one engulfs the lower one at $Z^* \approx 10^{-2}$.

From then on, the developing process is pretty much similar to that of $Gr = 10^6$. Since the buoyancy effect is much larger in this case, the secondary motion
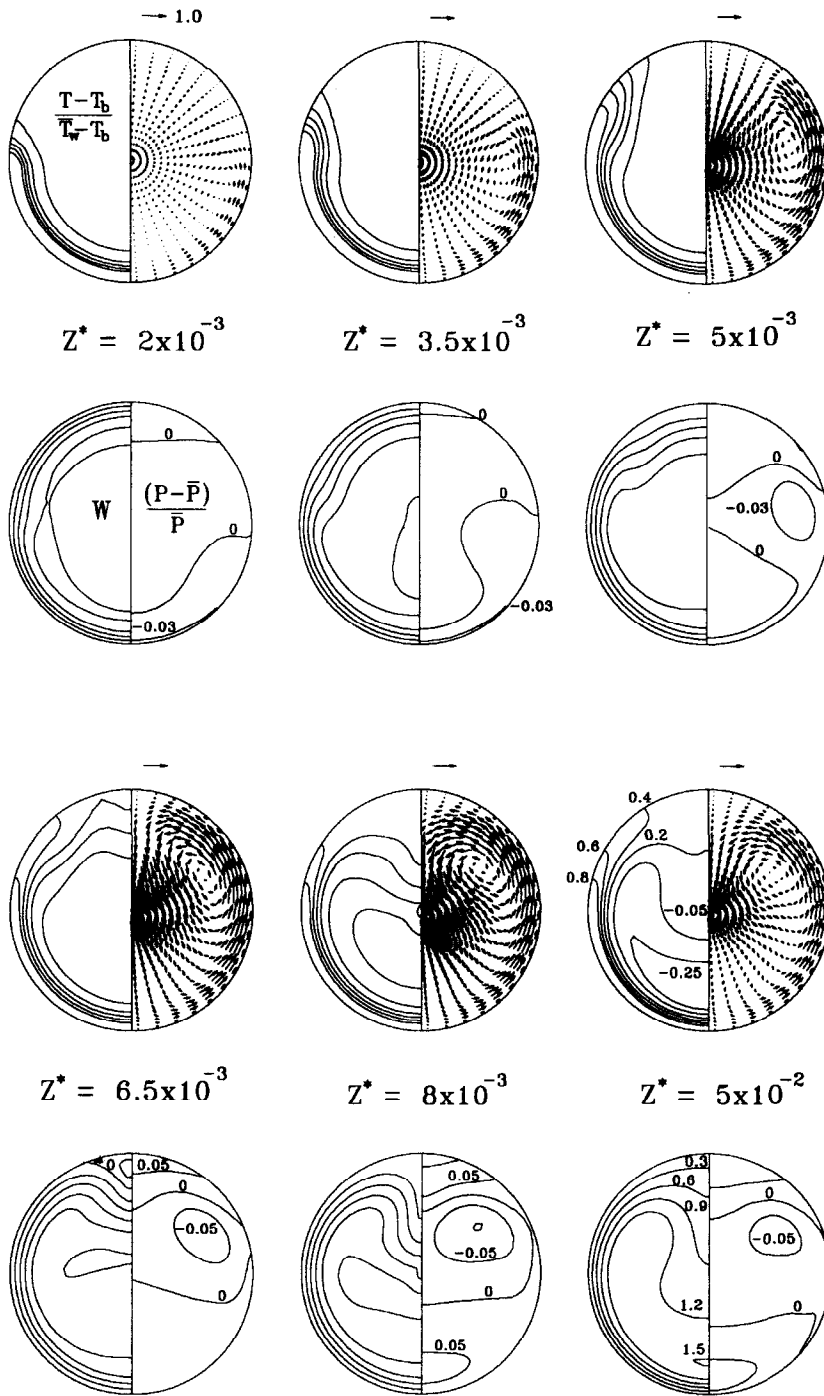
FIG. 5. Flow development of two-vortex solution for $Pr = 0.7$, $Gr = 10^6$.

is correspondingly stronger. The strong secondary motion helps mixing and results in a more uniform temperature field and weaker driving force. The clear oscillatory behavior of $f$ and $\overline{Nu}$ shown in Fig. 4 reflects this fluctuation in secondary motion, which was mentioned earlier.

The development of the flow at $Gr = 10^6$ for $Pr = 5$ is shown next in Fig. 8. The vortex formation and its development are qualitatively similar to those of $Pr = 0.7$ until $Z^* = 1.5 \times 10^{-3}$. After the vortex sweeps over the cross-section to the top, the secondary motion decreases as the mixing of the flow takes effect,
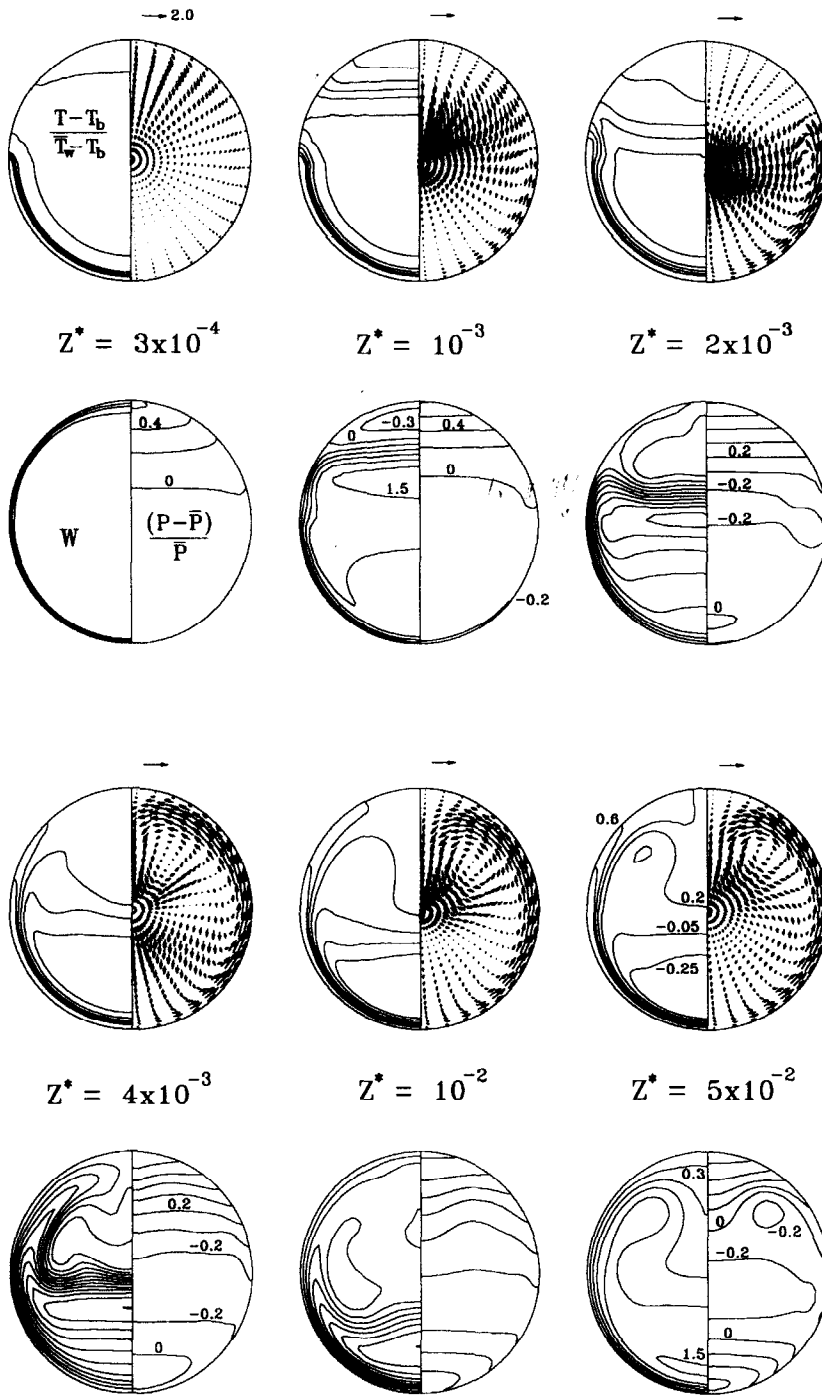
FIG. 6. Flow development of two-vortex solution for $Pr = 0.7$, $Gr = 10^7$.

i.e. reduction in buoyancy force : the flow in the upper region $(Z^* = 3 \times 10^{-3})$ and subsequently in the core region $(Z^* = 4.5 \times 10^{-3})$ slows down. The strength of the secondary flow is, in general, weaker than that for $Pr = 0.7$. This is because the thermal boundary layer is thin and, as a result, the fluid in the core region becomes stably stratified. The active secondary flow is confined to a small region close to the wall as the flow develops fully. The less vigorous motion restricts mixing and, hence, the flow attains a higher maximum axial velocity.

To illustrate how the flow bifurcates to a four-vor-
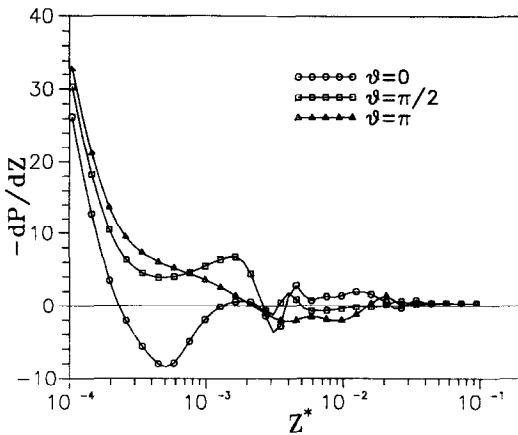
FIG. 7. Pressure gradient along three meridian sections for
$Pr = 0.7, Gr = 10^7$.

tex type, the flow developments downstream of the bifurcation point are shown in Fig. 9 for $Pr = 5$ and $Gr = 5 \times 10^6$. The four-vortex solution may successfully be obtained by disturbing the initial guess: the solution of the two-vortex flow is inverted and then fed in at the start of calculation. Although the values of $\overline{Nu}$ begin to show some difference at $Z^* = 4 \times 10^{-3}$ in Fig. 4, the crossflow pattern there remains unchanged in Fig. 9. However, as the crossflow along the tube surface in the bottom region slows down, a very strong temperature gradient in the vertical direction, i.e. along the symmetry plane, builds up. There seems to be a point where the two-vortex secondary flow is only neutrally stable: if the fluid particle near the bottom maintains its direction, the resulting flow is of two-vortex type that we have seen: however, any tilt toward the vertical direction results in a totally different flow type as this vertical motion is self-sustaining. This vertical convection process heats up the fluid in the plane of symmetry and thus increases the buoyancy force in that direction. This draws fluid from the side and forms another pair of vortices, i.e. a four-vortex crossflow pattern.

The bifurcation is expected to occur more readily as the buoyancy effect, i.e. $Gr$, increases as shown in Fig. 4. It is also evident from the figure that the increasing $Pr$ enhances the bifurcation to four-vortex pattern. The secondary motion and mixing in the higher $Pr$ flow are weak and thus the fluid close to the wall carries less momentum. This, coupled with the much higher unstable temperature gradient in the bottom region due to the thinner thermal boundary layer, makes the flow more susceptible to instability. The flow change in the lower part of the duct causes the friction factor and the Nusselt number to rise from those of the two-vortex type. Here again the flow oscillates due to the fluctuating buoyancy force until it gets fully developed.

The overall flow development may be summed up

nicely in a perspective view of the skin-friction coefficient $C_f$ and the Nusselt number $Nu$.

$$C_f = \frac{\tau_w}{\frac{1}{8}\rho \bar{w}^2} \quad Nu = \frac{qD}{k(T_w - T_b)} \quad (28)$$

where $\tau_w$ is the wall shear stress in the axial direction. $Nu$ is meaningful only in the lower half of the duct.

The results for $Pr = 0.7$ at $Gr = 10^6$ are shown in Fig. 10a. Near the inlet, the buoyancy effects are negligible and $C_f$ and $Nu$ decrease uniformly as in the forced convection boundary-layer flow. The first sign of the buoyancy effect appears in the $C_f$ plot as a local minimum near $\theta = \pi/2$. This point coincides with the point where the secondary flow loses its upward momentum and reverses direction (see Fig. 5). What happens is that the local fluid there is replaced by the lower momentum fluid from below: consequently, the axial velocity is reduced along with the skin friction. Since the vortex moves upward and gathers its strength as it travels downstream, the position of local minimum in $C_f$ moves upward ($\theta$ decreases) and the valley gets deeper as $Z$ increases. Before developed fully, the flow near the bottom accelerates due to the momentum transfer by the secondary flow; this also reduces the wall temperature ($T_w$) and raises $Nu$ in the region.

The friction-factor and Nusselt-number distributions for $Gr = 10^7$ are presented in Fig. 10b. The main difference in the $C_f$ distribution from that for $Gr = 10^6$ is a much stronger acceleration close to the vortex center near $\theta = \pi/2$. The axial flow deceleration in the upper part of the duct is similar but more pronounced. Hence, a larger and stronger reversed flow region is formed. Moreover, the strong acceleration near the vortex center makes the flow decelerate in the lower part as well as in the upper part to satisfy the continuity constraint. With increasing $Z$, the point of maximum $C_f$ moves downward ($\theta$ increases) in accordance with the position at which the axial velocity becomes maximum. The peak is shown near $Z^* = 10^{-2}$ at the bottom of the duct. The strong axial velocity there enhances heat transfer and, consequently, $Nu$ is also largest near that position.

The two- and four-vortex solutions for $Pr = 5$ at $Gr = 5 \times 10^6$ are compared in Fig. 11. The two-vortex solution is qualitatively similar to that of $Pr = 0.7$ and $Gr = 10^6$ except for the relatively large circumferential variation. The four-vortex solution, on the other hand, shows clearly the effects of the second vortex near the bottom: the distributions of $C_f$ and $Nu$ have been altered significantly in that region. As the flow develops to its final state, the $C_f$ and $Nu$ values behave similarly: the vortex motion that moves high momentum cold fluid from the core to the bottom makes both parameters increase. The peak value of $Nu$ is nearly twice as large as that of the two-vortex solution. The $Nu$ distribution has two peaks before they merge into one as the flow gets fully developed.
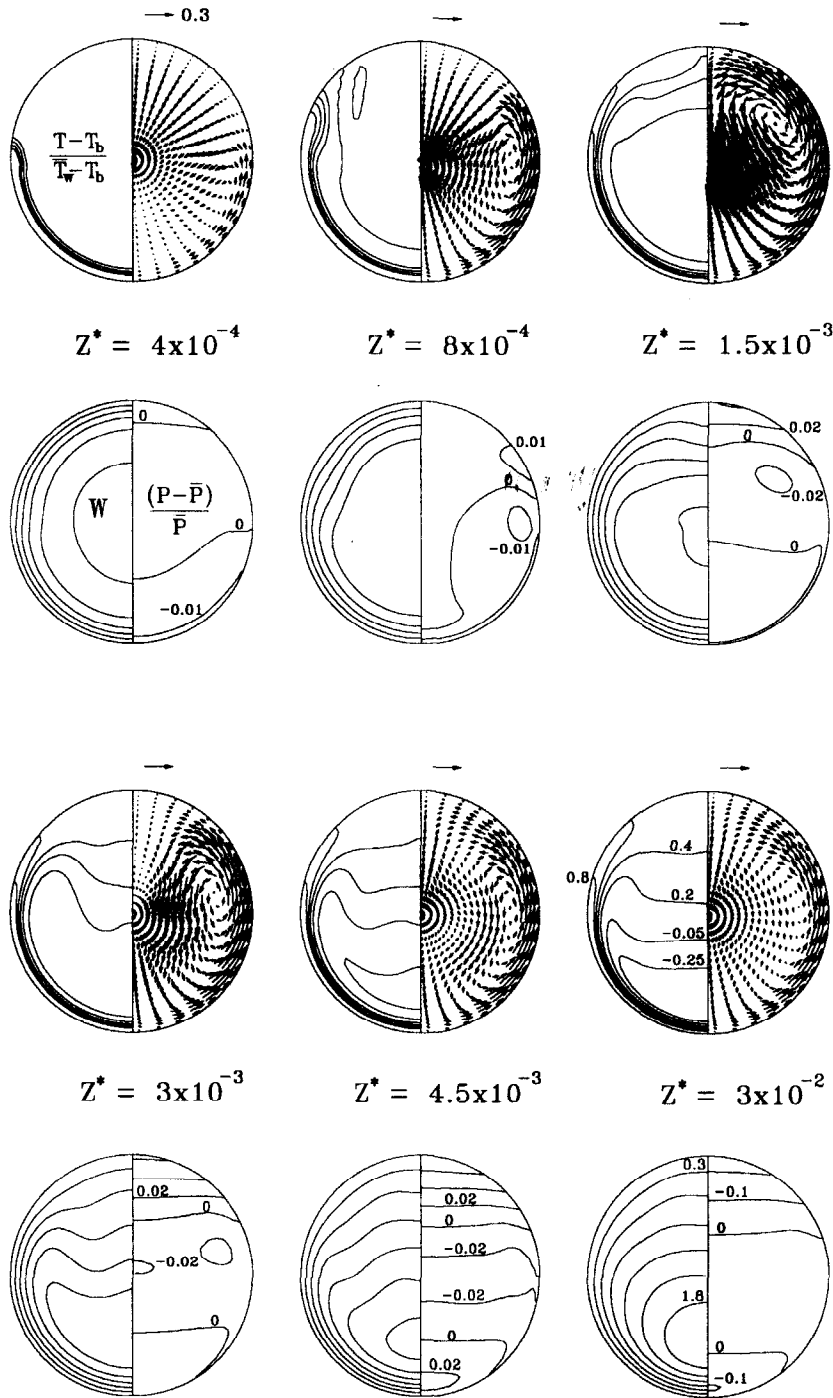
FIG. 8. Flow development of two-vortex solution for $Pr = 5$, $Gr = 10^6$.

The process can also be observed in the isotherms in Fig. 9, in which the temperature gradient normal to the surface shows two distinct peak values.

### SUMMARY

The developing mixed convection flow in a horizontal circular tube, the top half of which is insulated and the bottom half maintained at the constant heat-flux condition has been investigated. The fully elliptic 3-D Navier–Stokes equations together with the continuity and energy equations are solved by a modified SIMPLER algorithm. The global continuity at each cross-section in the flow is ensured by applying corrections to the axial velocity and the bulk pressure.
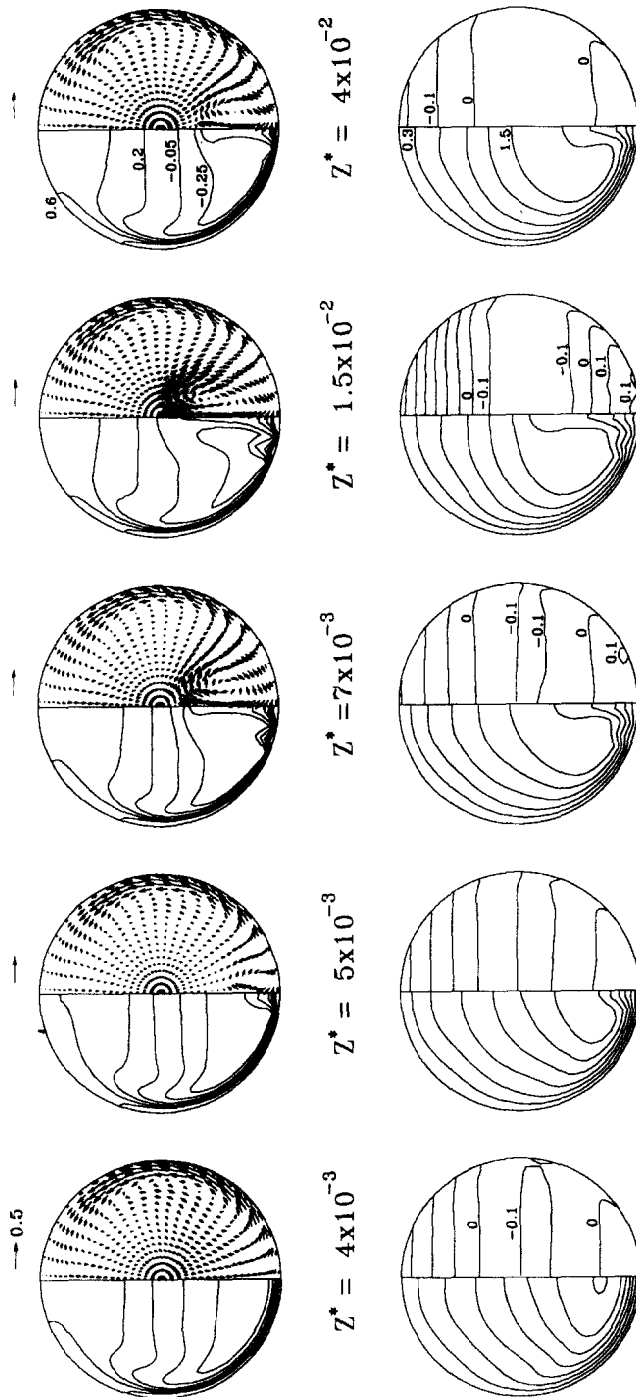
FIG. 9. Flow development of four-vortex solution for $Pr = 5$, $Gr = 5 \times 10^6$.
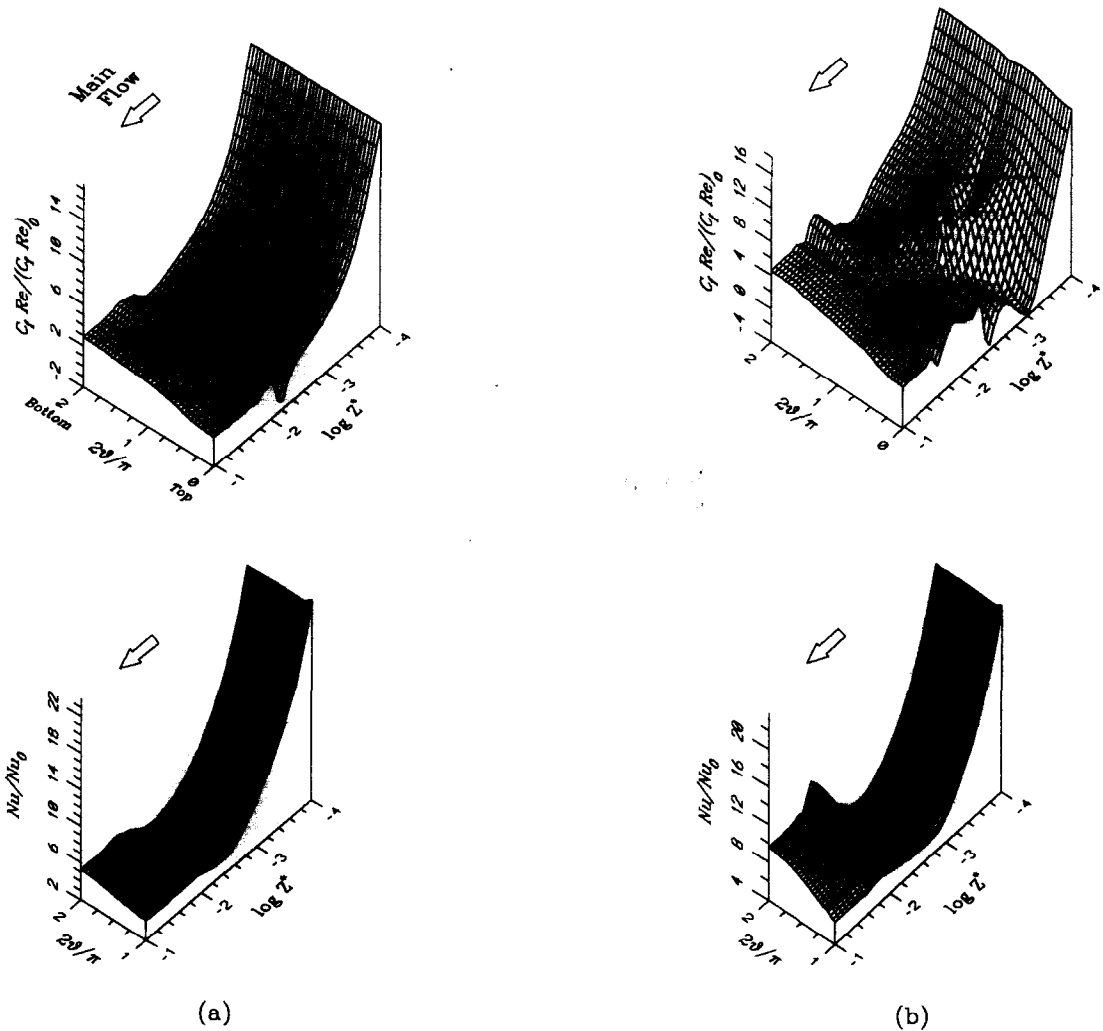
FIG. 10. Local friction factor and Nusselt number of two-vortex solution for $Pr = 0.7$: (a) $Gr = 10^6$, and (b) $Gr = 10^7$.

Comparing it with the standard SIMPLER algorithm, the procedure is found more efficient and robust for various cases tested.

The secondary flow develops almost immediately for the $Re$–$Gr$ combinations that have been examined. The crossflow motion begins with the ascending thermal plume along the wall. This disrupts the thermal boundary layer and, therefore, the heat transfer is enhanced. The average Nusselt number of the section, $\overline{Nu}$, that decreases initially because of the thermal boundary-layer growth, starts to rise as the secondary flow becomes more active. The ups and downs of the buoyancy force due to unstable stratification and subsequent mixing make the mean Nusselt number and friction factor oscillate before settling to the fully developed values.

The developing processes start out similarly for both $Pr = 0.7$ and 5 except that the secondary flow of the latter is weaker. Approaching to the fully developed state, however, the secondary motion in the core region diminishes and the temperature outside the thermal boundary layer becomes stably stratified for $Pr = 5$.

The bifurcation to a four-vortex flow is possible when the radial temperature gradient near the bottom surface becomes sufficiently large. Only then can the disturbance in the vertical direction be sustained and develop into a secondary vortex. For a given Reynolds number, the four-vortex flow is more likely to occur as $Gr$ and/or $Pr$ increase(s). Increasing $Gr$ makes the buoyancy force larger whereas raising $Pr$ hinders mixing and helps the temperature gradient to rise. Also for high $Gr$ ($\geqslant 10^6$ for $Pr = 0.7$ and $\geqslant 2 \times 10^6$ for $Pr = 5$), large buoyancy effects cause the flow to reverse along the top surface; the massive reversed flow makes the flow develop quite differently from that without it.

The present paper demonstrates successfully how the flow eventually develops to either of the two final
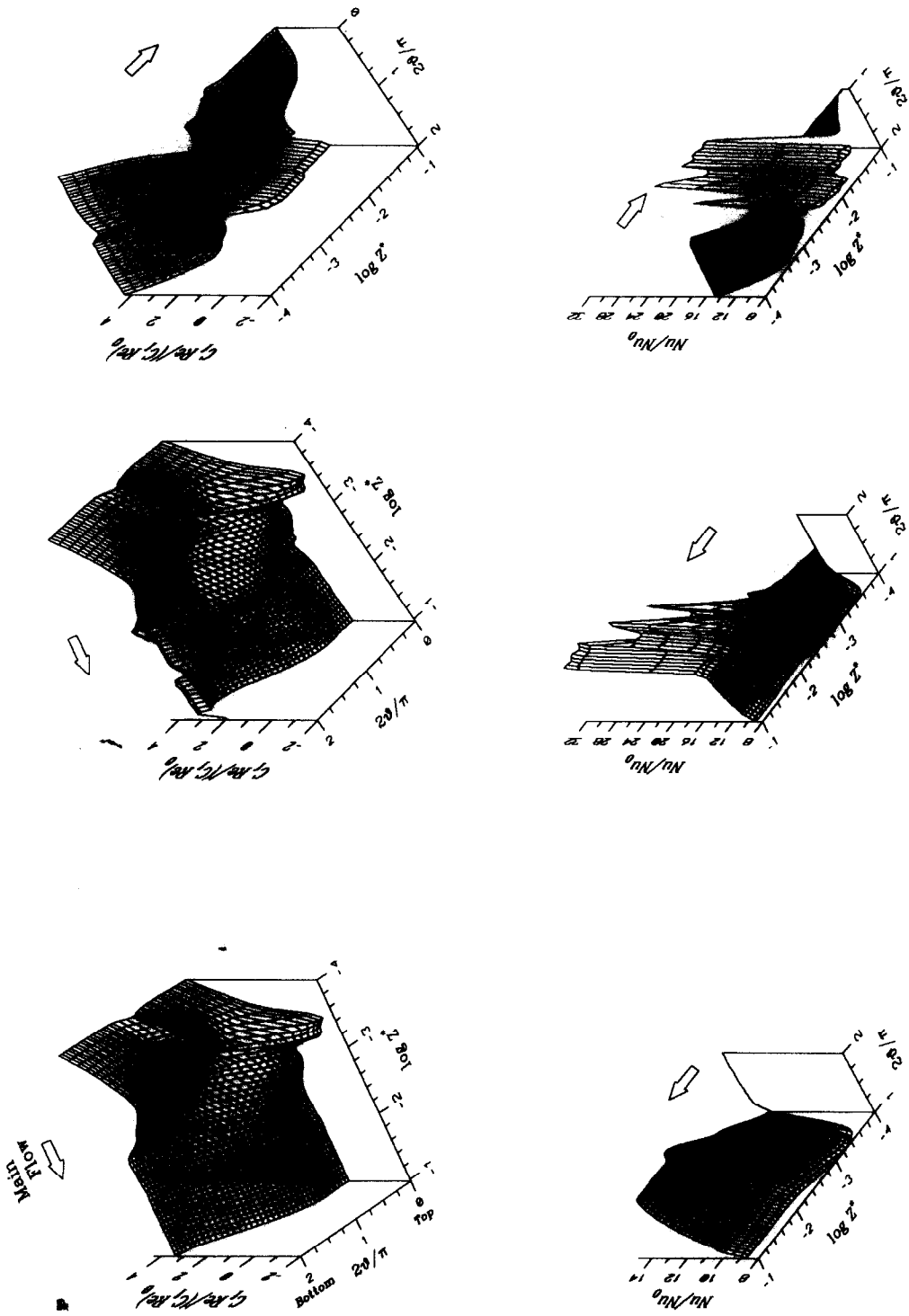
(a)

(b)

Fig. 11. Local friction factor and Nusselt number for $Pr = 5$, $Gr = 5 \times 10^6$: (a) two-vortex solution; and (b) four-vortex solution.

states, i.e. two- or four-vortex flow; this also verifies that, for a certain Grashof number range, both flows do occur.

## REFERENCES

1. K. C. Cheng and G. J. Hwang, Numerical solution for combined free and forced laminar convection in horizontal rectangular channels, *J. Heat Transfer* **91**, 59–66 (1969).
2. P. H. Newell and A. E. Bergles, Analysis of laminar combined free and forced convection for fully developed laminar flow in horizontal tubes, *J. Heat Transfer* **92**, 83–93 (1970).
3. F. C. Chou and G. J. Hwang, Combined free and forced laminar convection in horizontal rectangular channels for high *ReRa*, *Canadian J. Chem. Engng* **62**, 830–836 (1984).
4. K. Nandakumar, J. H. Masliyah and H. S. Law, Bifurcation in steady laminar mixed convection flow in horizontal ducts, *J. Fluid Mech.* **152**, 145–161 (1985).
5. J. H. Masliyah, On laminar flow in curved semi-circular ducts, *J. Fluid Mech.* **99**, 469–479 (1980).
6. K. Nandakumar and J. H. Masliyah, Bifurcation in steady laminar flow through curved tubes, *J. Fluid Mech.* **119**, 475–490 (1982).
7. S. V. Patankar, S. Ramadhyani and E. M. Sparrow, Effect of circumferentially nonuniform heating on laminar combined convection in a horizontal tube, *J. Heat Transfer* **100**, 63–70 (1978).
8. H. S. Law, J. H. Masliyah and K. Nandakumar, Effect of nonuniform heating on laminar mixed convection in ducts, *J. Heat Transfer* **109**, 131–137 (1987).
9. D. K. Choi and D. H. Choi, Dual solution for mixed convection in a horizontal tube under circumferentially non-uniform heating, *Int. J. Heat Mass Transfer* **35**, 2053–2056 (1992).
10. J. W. Ou, K. C. Cheng and R. C. Lin, Natural convection effects on Graetz problem in horizontal rectangular channels with uniform wall temperature for large *Pr*, *Int. J. Heat Mass Transfer* **17**, 835–847 (1974).
11. M. M. M. Abou-Ellail and S. M. Morcos, Buoyancy effects in the entrance region of horizontal rectangular channels, *J. Heat Transfer* **105**, 924–928 (1983).
12. H. V. Mahaney, F. P. Incropera and S. Ramadhyani, Development of laminar mixed convection in a horizontal rectangular duct with uniform bottom heating, *Numer. Heat Transfer* **12**, 137–155 (1987).
13. H. V. Mahaney, F. P. Incropera and S. Ramadhyani, Effect of wall heat flux distribution on laminar mixed convection in the entrance region of a horizontal rectangular duct, *Numer. Heat Transfer* **13**, 707–729 (1988).
14. D. Choudhury and S. V. Patankar, Combined forced and free convection in the entrance region of an inclined isothermal tube, *J. Heat Transfer* **110**, 901–909 (1988).
15. M. Hishida, Y. Nagano and M. S. Montesclaros, Combined forced and free convection in the entrance region of an isothermally heated horizontal pipe, *J. Heat Transfer* **104**, 153–159 (1982).
16. C. G. Yam and H. A. Dwyer, Combined forced and free convection in a curved duct, *Fifth Symposium on Numerical and Physical Aspects of Aerodynamic Flow* (1992).
17. M. Hishida, Y. Nagano and H. Aiki, Free convection effects on laminar flow in the entrance region of a horizontal pipe (2nd report, uniform wall heat flux), *Trans. JSME(B)* **50**, 2171–2178 (1984).
18. S. V. Patankar, *Numerical Heat Transfer and Fluid Flow*. McGraw-Hill, New York (1980).
19. D. G. Lilley and D. L. Rhode, A computer code for swirling turbulent axisymmetric recirculating geometries, NASA CR-3442 (1982).
20. Y. S. Chen, A computer code for three-dimensional incompressible flows using nonorthogonal body-fitted coordinate systems, NASA CR-178818 (1986).
21. G. D. Raithby and G. E. Schneider, Numerical solution of problems in incompressible fluid flow: treatment of the velocity–pressure coupling, *Numer. Heat Transfer* **2**, 417–440 (1979).
22. Pratap, Flow and heat transfer in curved ducts, Ph.D. Thesis, Imperial College (1975).
23. B. P. Leonard, A stable and accurate convective modelling procedure based on quadratic upstream interpolation, *Computer Methods Appl. Mech. Eng.* **19**, 59–98 (1979).